Layering Transitions in Thin Films of Spherical-Domain Block Copolymers

Gila E. Stein,[†] Edward J. Kramer,*[,†,‡] Xuefa Li,[§] and Jin Wang[§]

Department of Chemical Engineering, University of California, Santa Barbara, California 93106; Department of Materials, University of California, Santa Barbara, California 93106; and Advanced Photon Source, Argonne National Laboratory, Argonne, Illinois 60439

Received November 5, 2006; Revised Manuscript Received December 10, 2006

ABSTRACT: Highly asymmetric block copolymers forming spherical microdomains arrange in a hexagonal lattice as a monolayer, while the bulk equilibrium structure is body-centered cubic. We report a complex transition from two- to three-dimensional packing in thin films of spherical-domain poly(styrene-*b*-2vinylpyridine), measured by grazing-incidence small-angle X-ray scattering and transmission electron microscopy. The monolayer hexagonal symmetry persists through three layers, with close-packed AB and ABA stacking in films two and three layers thick. At four layers, coexistence between an equilibrium hexagonal close-packed symmetry and a metastable face-centered orthorhombic structure is observed. As the number of layers is further increased from 4 to 23, the hexagonal phase vanishes, and the symmetry of the face-centered orthorhombic phase deforms to approach asymptotically a structure similar to a body-centered cubic lattice with the closest-packed (110) plane oriented parallel to the substrate. Self-consistent-field theory calculations demonstrate that these thickness-dependent packing symmetries result from a competition between the packing preferred in the bulk with that at the interfaces.[1]

Introduction

The physics of bulk diblock copolymer melts are well understood, where the equilibrium phase behavior is determined by chain stretching and interfacial energy contributions to the total free energy. Below an order−disorder transition, a range of composition-dependent two- and three-dimensional periodic morphologies are observed.[2] However, the structure in thin films may differ from the bulk as a consequence of both geometric frustration and surface interactions. These confinement effects are most thoroughly studied for the lamellar morphology observed in volume symmetric systems,[3] where the domain orientation is largely determined by the surface energy of the blocks at each boundary. For a typical case of symmetric boundary conditions, such as confinement between two hard walls, the preferential attraction of one block to the interface induces layering parallel to the boundaries. If the wall separation is incommensurate with a multiple of the equilibrium lamellar periodicity, frustrated structures can result despite the entropic penalty for compressing or stretching the domain.[4] A more technologically relevant system is realized in substrate supported films, a form of asymmetric boundary conditions. In these systems, the surface energy and substrate interfacial energy of a given block are not necessarily equal, and an extra half-lamellae is produced at one or both interfaces.[5] When the film thickness is incommensurate with the stable configuration, relief structures form at the free interface in the form of islands of excess material or depletion holes to relieve entropic frustration. The film then consists of regions with two distinct thicknesses that are commensurate with the equilibrium domain periodicity.[6,7]

Many of the findings from symmetric block copolymers are relevant for asymmetric systems forming morphologies with curved interfaces. For example, asymmetric block copolymers can exhibit lamellar-like wetting layers induced by strong surface or substrate interactions, despite the entropic penalty associated with producing a flat interface.[8] Strong layering parallel to the substrate is typically observed in systems forming cylindrical domains,[9] as well as in systems of spherical domains,[10] and terraced structures form when the as-cast film thickness is incommensurate with the equilibrium periodicity.[11] However, when a block copolymer system forming a three-dimensional morphology in bulk is confined to a quasi-two-dimensional thin film, another degree of geometric frustration is introduced. This is exemplified by highly asymmetric block copolymers forming spherical domains, where the body-centered cubic (BCC) symmetry is stable in bulk and hexagonal (HEX) symmetry is preferred by the monolayer. The BCC lattice in three dimensions and the HEX lattice in two dimensions minimize packing frustration, which arises from competition between stretching and interfacial energies: The interfacial energy is minimized when the interfacial curvature is uniform, while the stretching energy is minimized by uniform extension of the chains.[12,13] These constraints cannot be simultaneously satisfied, so the equilibrium lattice reflects the packing arrangement that minimizes variations in the domain thickness.[14]

The transition from two- to three-dimensional packing in spherical-domain block copolymers has not been explored, largely due to the absence of a suitable experimental technique for measuring such structures. The most relevant work to date employed dynamic secondary ion mass spectrometry to depth profile multilayered films. Strong ordering of the spheres normal to the substrate was reported, with layer thicknesses consistent with the periodicity of the BCC (110) plane.[10] Measurements of the lateral structure at the free surface by scanning force microscopy resembled the symmetry of the BCC (110) plane.[15] The (110) plane is the closest-packed in the BCC lattice, resembling a "distorted" hexagonal lattice, and this preferential orientation minimizes frustration at the free and substrate interfaces. Therefore, we might expect to see this symmetry mediate the transition from two to three dimensions.

* Corresponding author. E-mail: edkramer@mrl.ucsb.edu.
† Department of Chemical Engineering, UCSB.
‡ Department of Materials, UCSB.
§ Argonne National Laboratory.

10.1021/ma0625509 CCC: $37.00
Published on Web 03/03/2007

In this paper, grazing-incidence small-angle X-ray scattering (GISAXS) is used to measure the lattice symmetry in silicon-supported films having 1−23 layers. This relatively new technique is ideally suited for probing the structure with high accuracy and provides a statistically meaningful measure of the structure. (The illuminated area is on the order of 1 mm^2, as compared with direct measurements of the lattice by microscopy, which measures ~1 μm^2.) We present a simple methodology for structural analysis: First, the in-plane symmetry is determined by fitting the in-plane scattering data to a two-dimensional lattice model. A basis is then assumed to describe the stacking of layers perpendicular to the substrate, and the GISAXS pattern is simulated for comparison with the experimental data. This approach is complemented by direct measurement of the lattice with transmission electron microscopy. We find that hexagonal close-packed symmetry breaks to form a face-centered orthorhombic phase when the number of layers is increased from four to five. As the number of layers is further increased from five, the in-plane symmetry of the orthorhombic unit cell deforms to discretely approach a structure similar to the BCC lattice with the (110) plane parallel to the substrate.

Experimental Procedures

Polymer System. Poly(styrene-*b*-2vinylpyridine) (PS−PVP) was synthesized by anionic polymerization, producing a polydispersity index of 1.04, an overall degree of polymerization $N = 626$, and a composition of 12 vol % PVP. The PVP minority block forms spherical domains in a PS matrix. Small-angle X-ray scattering from bulk samples demonstrates the expected body-centered cubic morphology, and scanning force microscopy measurements of the monolayer structure are consistent with hexagonal symmetry (not shown). The scattering length densities of PS and PVP were measured by X-ray reflectivity and are $9.5 \times 10^{-10}/cm^2$ and $10.1 \times 10^{-10}/cm^2$, respectively.

Sample Preparation for GISAXS. Thin films of PS−PVP ranging from 40 nm to 0.5 μm thick (1−23 layers) were prepared by spin-casting from 1−9 wt % toluene solutions onto 5 mm thick silicon substrates. The silicon was cleaned prior to spin-casting with Piranha solution (2.5:1 H_2SO_4/30 wt % H_2O_2 by volume) to destroy any organic contamination. Precautions undertaken when handling Piranha included wearing a full face shield, acid resistant apron, and heavy-duty rubber gloves. All films were annealed under high vacuum (10^{-7} Torr) to order the structure according to two thermal profiles: (1) a direct anneal, consisting of a short heating period followed by a 3 day anneal at 215 ± 5 °C; and (2) slow cooling from 275 ± 5 °C through the order−disorder transition at 250 ± 7 °C ($\chi N_{ODT} \approx 54$) to 215 ± 5 °C ($\chi N \approx 60$), followed by a 3 day anneal at 215 ± 5 °C. The PVP block wets the native oxide at the silicon surface, producing a brush layer. The layers of spheres form on top of the brush. Typically, the as-cast film thickness is incommensurate with the equilibrium layer thickness, so a low density of island or hole relief structures is observed at the free interface. The number of layers per sample was determined by depth profiling with secondary ion mass spectrometry (SIMS), using the O_2^+ beam at a voltage of 2 kV, current of 60 nA, and a raster area of 0.07 mm^2. Charge compensation was provided by a static 600 V electron beam. Negative ions of C^-, CN^-, and Si^- were monitored as a function of time, where the CN^- signal is unique to the PVP domains. Strong layering of the PVP domains perpendicular to the substrate is observed, consistent with previous reports. The layer thickness a_{layer} (required for GISAXS simulations) is approximately determined from reflectivity measurements on films having $n = 1-8$ layers, using a Philips X'Pert MRD operating at a wavelength of 0.154 nm (Cu Kα). The reflectivity for each sample was fit following the Parratt formalism to obtain the *total* film thickness as a function of the number of layers, $t(n)$.[16,17] This was fit to a linear profile $t(n) = a_{layer}n + b$, where the parameter a is the approximate layer thickness and the parameter b is the brush thickness. This results in $a_{layer} = 21.8 \pm 0.4$ nm and $b = 18 \pm 1$ nm.

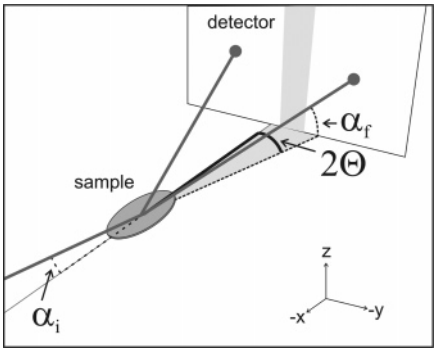

Figure 1. GISAXS geometry.

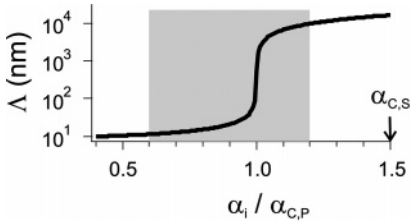

Figure 2. X-ray penetration depth Λ of polystyrene, for a film of semiinfinite thickness. The shaded region marks the range of incident angles used for this study.

Grazing Incidence Small-Angle X-ray Scattering. Grazing incidence small-angle X-ray scattering (GISAXS) experiments were conducted at the XOR Beamlines 1-BM-C and 8-ID-E at the Advanced Photon Source (APS) of Argonne National Laboratory, with X-ray energies of 11.8 keV ($\lambda = 0.1042$ nm) and 7.5 keV ($\lambda = 0.1675$ nm) at the respective lines. The GISAXS geometry is illustrated in Figure 1. The sample is irradiated at a fixed incident angle α_i on the order of a tenth of a degree, and the off-specular scattering is recorded with a 2D MAR-CCD detector. The strong specular reflection from the samples is blocked by a lead beam stop. The resulting data set is a map of intensity $I(2\Theta,\alpha_f)$, where 2Θ is the in-plane diffraction angle and α_f is the out-of-plane diffraction angle. Each data set is stored as a 2048 × 2048 16-bit TIFF image.

For these experiments, the incident angle α_i was varied about the critical angle of the polymer $\alpha_{C,P}$ in the range $0.6 \leq \alpha_i/\alpha_{C,P} < 1.2$. This produces controlled penetration depths ranging from ~10 nm, where only the top layer of spheres is measured, up to the full film thickness.[18] The sharp increase in X-ray penetration depth near the critical angle of polystyrene is illustrated in Figure 2. All incident angles were below the critical angle for silicon, which is $\alpha_{C,S} = 1.5\alpha_{C,P}$. Typical individual exposure times ranged from 10 to 40 s, and several measurements from each incident angle were summed to provide a signal well above the background.

For analysis, the summed data sets were converted from the 2048 × 2048 images to $(2\Theta,\alpha_f)$ coordinates. This conversion is a function of the detector resolution ρ and the sample-to-detector distance ξ. The detector pixel size for all runs was 79 μm. The sample-to-detector distance for each run was calibrated with a silver behenate standard ($d = 58.376$ Å). The diffraction angles $(2\Theta,\alpha_f)$ are calculated from eqs 1 and 2, where (x_b,y_b) denotes the coordinate of the beam center in pixels.

$$2\Theta = \arctan\left(\frac{\rho(x - x_b)}{\xi}\right) \quad (1)$$

$$\alpha_f = \arctan\left(\frac{\rho(y - y_b)}{\xi}\right) - \alpha_i \quad (2)$$

Within the small-angle approximation, $(2\Theta,\alpha_f) \propto 1/\xi$. Therefore, the error associated with calibration of ξ is virtually eliminated by

measuring the ratio of peak positions, which is particularly important when comparing data from multiple runs and beamlines.

The incident angle α_i was calibrated by $\theta-2\theta$ scans in the specular plane with a pin diode point detector. This results in errors on the order of $\pm 0.01°$, which are measured as follows: The specular reflection from a silicon wafer is recorded with the 2D detector for a range of incident angles. The position of the specularly reflected beam in α_f is compared to the expected value calculated by eq 2 to determine the deviation. The following sections review why this error is significant and how to account for it during data analysis.

Transmission Electron Microscopy. Samples were prepared as follows: A 200 nm thick layer of SiO_2 was deposited onto silicon wafers by plasma-enhanced chemical vapor deposition. Thin films of PS−PVP ranging from three to six layers thick were spun-cast on top of the silicon oxide and annealed under high vacuum by slow cooling at a rate of 0.046 °C/min from 275 ± 5 °C followed by a 4 day anneal at 215 ± 5 °C. Upon removal from the oven, samples were rapidly quenched below the glass transition temperature of both PS and PVP to freeze the structure. The film was then floated off of the silicon substrate onto a TEM grid in a 25 wt % HF solution, which etches away the oxide layer to free the polymer film from the substrate. Precautions undertaken when handling the HF solution included wearing a full face shield, acid-resistant apron, and heavy-duty rubber gloves. Samples were exposed to iodine vapor at room temperature for ∼1 h to stain the PVP domains prior to measurement by TEM. Measurements were completed with a FEI Tecnai G20 operating at 200 kV. Samples were imaged at several tilt angles normal to the substrate, and the resulting projections were compared with simulations to determine the three-dimensional lattice symmetry.

GISAXS Analysis

GISAXS Scattering Vectors. Thin films of spherical-domain block copolymers form periodic layers parallel to the substrate,[10] so analysis is restricted to the case where diffracting crystallographic planes are perpendicular to the substrate. The incident and diffracted wave vectors inside the film, corrected for refraction at the air−polymer interface, are denoted as $\mathbf{k}_i$ and $\mathbf{k}_f$, and calculated as follows:

$$\mathrm{k_i} = k(\cos\alpha_i,\ 0,\ -\sqrt{n^2 - \cos^2\alpha_i}) \tag{3}$$

$$\mathrm{k_f} = k(\cos\alpha_f \cos 2\Theta,\ \cos\alpha_f \sin 2\Theta,\ \sqrt{n^2 - \cos^2\alpha_f}) \tag{4}$$

The parameter n is the complex index of refraction for the polystyrene matrix, and k is the wave vector modulus $2\pi/\lambda$. Calculation of the in-plane scattering vector q_{par} is straightforward:

$$q_{par} = \sqrt{q_x^{\,2} + q_y^{\,2}} \tag{5}$$

$$q_x = k_{f,x} - k_{i,x} \tag{6}$$

$$q_y = k_{f,y} - k_{i,y} \tag{7}$$

However, calculation of the out-of-plane scattering vector is considerably more complex. Above the critical angle of the polymer, the theoretical maximum penetration depth (calculated for a semiinfinite film) is much larger than the film thickness of our samples. The transmitted wave can therefore be reflected at the polymer−substrate interface in combination with diffraction from the microstructure. Under the assumptions that each ray scatters no more than once from the spheres (the kinematic approximation) and there is no transmission through the substrate ($\alpha_i < \alpha_{C,S}$), there are four possible scattering events to be considered. Such single-scattering events with reflection from the substrate are illustrated in Figure 3, and the corresponding out-of-plane scattering vectors are calculated by eqs 8−11.

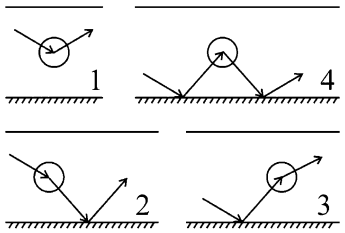

Figure 3. Four scattering events, demonstrating different combinations of reflection from the substrate with diffraction from the microstructure.

$$q_{z,1} = k_{f,z} - k_{i,z} \tag{8}$$

$$q_{z,2} = -k_{f,z} - k_{i,z} \tag{9}$$

$$q_{z,3} = k_{f,z} + k_{i,z} \tag{10}$$

$$q_{z,4} = -k_{f,z} + k_{i,z} \tag{11}$$

The approach taken to determine the lattice symmetry is designed to simplify much of the out-of-plane analysis. First, the position of the in-plane peaks is fit to a 2D model, thereby obtaining the in-plane symmetry. Then a basis is assumed to describe stacking of layers out-of-plane, and the $I(2\Theta,\alpha_f)$ scattering is simulated for comparison with the experimental data.

In-Plane Analysis. For each measurement, line integrations are performed to extract $I(2\Theta)$ profiles from the two-dimensional data sets. The position of the line integration in α_f is somewhat arbitrary but is always in the range $\alpha_{C,P} < \alpha_f < \alpha_{C,S}$ where the diffracted intensity is a maximum. The $I(2\Theta)$ data are converted to $I(q_{par})$ coordinates by eq 3. The background is subtracted using either the sum of a Gaussian and a Lorentzian function or a polynomial baseline, and the maxima in intensity are fit with Voigt functions to obtain the reciprocal space peak positions. For a hexagonal lattice, the ratio of in-plane reciprocal-space peak positions is $q^*:\sqrt{3}q^*:2q^*$, and for the BCC (110) plane the ratio is $q^*:\sqrt{4/3}q^*:\sqrt{8/3}q^*$, where q^* denotes the first observed reflection. While the packing in films 1−3 layers thick is consistent with the HEX phase, films thicker than three layers do not match either symmetry. For this reason, the data are fit to a general 2D model, which is described by eqs 12−14, and illustrated in Figure 4.

$$\mathbf{a}_1 = (a_1 \sin\phi,\ a_1 \cos\phi,\ 1) \tag{12}$$

$$\mathbf{a}_2 = (0,\ a_2,\ 1) \tag{13}$$

$$\mathbf{a}_3 = (0,\ 0,\ 1) \tag{14}$$

The in-plane reciprocal lattice vectors $\mathbf{b}_1$ and $\mathbf{b}_2$ are calculated in the usual way, with $\mathbf{b}_1 = 2\pi(\mathbf{a}_2 \times \mathbf{a}_3)/(\mathbf{a}_1 \cdot (\mathbf{a}_2 \times \mathbf{a}_3))$. The model scattering vector is $Q^m_{par} = h\mathbf{b}_1 + k\mathbf{b}_2$, where (h,k) are the 2D plane indices. The experimental peak positions q_{par} are fit to the model Q^m_{par} using a_1, a_2, and ϕ as adjustable parameters. All fits are implemented with a Levenberg−Marquardt algorithm to search for the values that minimize $\chi^2 = \sum_i(|Q^m_{par}| - |q_{par}|_i)^2/\sigma_i^2$ and calculate the standard deviation σ for each parameter.

Table 1. The Three Bases Considered To Describe Stacking of Layers

case	symmetry	x_1	y_1	z_1	x_2	y_2	z_2	x_3	y_3	z_3
1	HCP	0	0	0	1/3	1/3	1/2			
2	FCC	0	0	0	1/3	1/3	1/3	−1/3	1/3	2/3
3	FCO	0	0	0	1/2	0	1/2			

Out-of-Plane Analysis. The scattering for the four events illustrated in Figure 3 is simulated by the distorted-wave Born approximation (eq 6).[19−21] In this approximation, the electron density is calculated as the superposition of two terms, where one term describes a perfect sample that has no lateral variation in density and the second term describes the in-plane disturbance. The scattering from the perfect sample is calculated from dynamical theory, while scattering from the disturbance is treated kinematically.

$$I(2\Theta,\alpha_f) = \frac{1}{16\pi^2}|T_i T_f F(q_{par},q_{z,1}) + T_i R_f F(q_{par},q_{z,2}) + T_f R_i F(q_{par},q_{z,3}) + R_i R_f F(q_{par},q_{z,4})|^2 \quad (15)$$

The coefficients $T_i(\alpha_i)$, $T_f(\alpha_f)$, $R_i(\alpha_i)$, and $R_f(\alpha_f)$ are the amplitudes of the transmitted and reflected waves inside the film, where the subscripts i and f denote incoming and outgoing waves. These are calculated from dynamical theory by the Parratt recursions for layered systems.[16,17]

The scattering potential for the disturbance, $F(q_{par},q_z)$, is approximated as the product of the spherical form factor $P(q,q_z)$, the structure factor $S(\mathbf{q})$, and a geometric factor $G(\mathbf{q})$. The form factor utilized in these simulations describes perfect hard spheres with a radius of $R_s = 7.5$ nm (eq 7). The structure factor dictates which reflections are allowed and depends on the basis that describes the stacking of layers within the unit cell (eq 17). The geometric factor accounts for finite film thickness (eq 18).

$$P(q,q_z) = 4\pi {R_s}^3 \frac{\sin(qR_s) - qR\cos(qR_s)}{(qR_s)^3}\exp(-q_z R_s) \quad (16)$$

$$S(\mathbf{q}) = \sum_j e^{-\imath \mathbf{q}\cdot\mathbf{r}_j} \quad (17)$$

$$G(\mathbf{q}) = \sum_{n_1=-\infty}^{\infty} e^{\imath(n_1\mathbf{q}\cdot\mathbf{a}_1)} \sum_{n_2=-\infty}^{\infty} e^{\imath(n_2\mathbf{q}\cdot\mathbf{a}_2)} \sum_{n_3=0}^{N_3-1} e^{\imath(n_3\mathbf{q}\cdot\mathbf{a}_3)} \quad (18)$$

The limits for the summations in eq 18 denote the number of unit cells along the x, y, and z axes. In bulk samples, the sample is effectively infinite in every direction, and the function is sharply peaked at the Bragg points. For thin films, however, the number of unit cells is only infinite in x and y. Along the z axis, the finite number of unit cells N_3 produces crystal truncation rods,[22] where the Bragg peaks are elongated in α_f and connected by rods of nonzero intensity. This scattering along α_f is amplified near the critical angle of the polymer, a consequence of coherent interference between the transmitted and reflected waves inside the film (the Yoneda peaks).[23,24]

The DWBA is implemented by assuming a basis (x_j,y_j,z_j) to describe stacking of layers normal to the substrate. This is a trial-and-error process, but there are three logical starting points that are listed in Table 1: (1) a two-point basis to describe the hexagonal close-packed ABA symmetry (HCP, $P6_3/mmc$); (2) a three-point basis to describe close-packed ABC stacking of face-centered cubic (111) planes (FCC, $Fm3m$); and (3) a two-point basis to describe a face-centered orthorhombic ABA symmetry (FCO, $Fmmm$), which includes stacking of BCC (110) planes. The vectors $\mathbf{r}_j = x_j\mathbf{a}_1 + y_j\mathbf{a}_2 + z_j\mathbf{a}_3$ then describe the position of spheres within the unit cell. The three-dimensional lattice vectors a_1, a_2, and a_3 are calculated by eqs 19−21, where the parameters a_1, a_2, and ϕ were previously determined by fitting the in-plane symmetry. The parameter a_3 denotes the height of the unit cell along the z axis and depends on both the layer thickness ($a_{layer} \approx 22$ nm) and the assumed basis.

$$\mathbf{a}_1 = (a_1 \sin\phi,\ a_1\cos\phi,\ 0) \quad (19)$$

$$\mathbf{a}_2 = (0,\ a_2,\ 0) \quad (20)$$

$$\mathbf{a}_3 = (0,\ 0,\ a_3) \quad (21)$$

The scattering vector corresponding with the plane (h,k,l) is $\mathbf{q} = h\mathbf{b}_1 + k\mathbf{b}_2 + l\mathbf{b}_3$. While h and k are integers, the index l is a *continuous* variable, producing a maximum in $G(q_z)$ when l takes an integral value (the Bragg point).

The objective of the simulations is to produce an intensity map $I(2\Theta,\alpha_f)$ to compare with the experimental data, so the diffraction coordinates $(2\Theta,\alpha_f)$ are calculated for each value of $\mathbf{q}(h,k,l)$ by solving eqs 8−11 for $\alpha_f > 0$ and eq 3 for 2Θ. The degenerate solutions $\alpha_f^1 = \alpha_f^2 = \alpha_f^{(a)}$ and $\alpha_f^3 = \alpha_f^4 = \alpha_f^{(b)}$ simplify implementation of eq 6 by allowing computation to be split into two parts, detailed by eqs 22−27.

$$\alpha_f^{(a)} = \arcsin\sqrt{\left(\frac{q_z}{k}\right)^2 + \sin^2\alpha_i - \frac{2q_z}{k}\sqrt{n^2 - 1 + \sin^2\alpha_i}} \quad (22)$$

$$\alpha_f^{(b)} = \arcsin\sqrt{\left(\frac{q_z}{k}\right)^2 + \sin^2\alpha_i + \frac{2q_z}{k}\sqrt{n^2 - 1 + \sin^2\alpha_i}} \quad (23)$$

$$2\Theta^{(a,b)} = \arccos\left(\frac{\cos^2\alpha_f^{(a,b)} + \cos^2\alpha_i - (q_{par}/k)^2}{2\cos\alpha_f^{(a,b)}\cos\alpha_i}\right) \quad (24)$$

$$A^{(a)}(2\Theta^{(a)},\alpha_f^{(a)}) = T_i T_f F(q_{par},q_{z,1}) + T_i R_f F(q_{par},q_{z,2}) \quad (25)$$

$$A^{(b)}(2\Theta^{(b)},\alpha_f^{(b)}) = T_f R_i F(q_{par},q_{z,3}) + R_i R_f F(q_{par},q_{z,4}) \quad (26)$$

$$I(2\Theta,\alpha_f) = \frac{1}{16\pi^2}|A^{(a)}(2\Theta^{(a)},\alpha_f^{(a)}) + A^{(b)}(2\Theta^{(b)},\alpha_f^{(b)})|^2 \quad (27)$$

The $I(2\Theta,\alpha_f)$ data calculated from eq 27 are broadened in 2Θ-space by a Gaussian function with the form $\exp(-\pi {q_{par}}^2/w^2)$, the Warren line shape[25] with $w \approx 0.0013$ nm^{-1}, describing a grain size on the order of 1 μm.

GISAXS Results and Discussion

In-Plane Symmetry Transitions. The in-plane symmetry is quantified by three parameters that are illustrated in Figure 4a: the first-nearest-neighbor a_2, the second-nearest-neighbor a_1, and the lattice angle ϕ. Hexagonal symmetry is characterized by $a_1/a_2 = 1$ and $\phi = 60°$, and the symmetry of the BCC (110) by

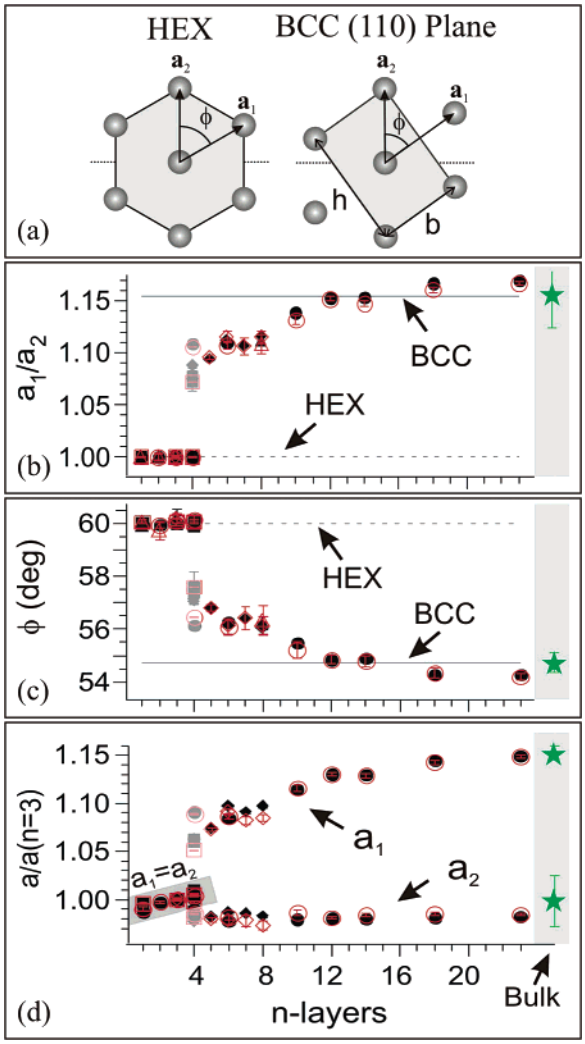

Figure 4. In-plane symmetry results as a function of the number of layers n in the film. (a) Illustration of model parameters for the HEX lattice and the symmetry of the BCC (110) plane. (b) Ratio of second-to-first nearest-neighbor $a_1(n)/a_2(n)$. (c) Lattice angle $\phi(n)$. (d) Magnitude of first- and second-nearest neighbors normalized by values for a trilayer sample, $a_2(n)/a_2(3)$ and $a_1(n)/a_1(3)$. The parameters measured from a bulk calibration sample in transmission mode are marked by the stars in the shaded region.

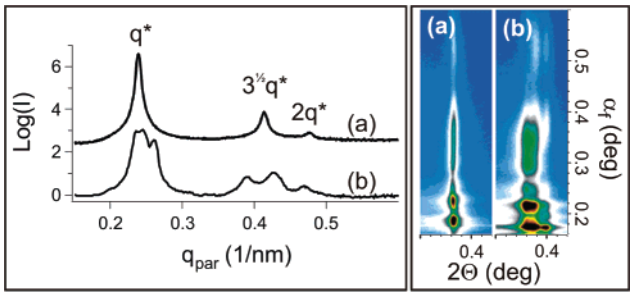

Figure 5. Experimental GISAXS $I(2\Theta,\alpha_f)$ data and in-plane line profiles for four layer samples, collected at $\alpha_i = 1.15\alpha_{C,P}$, $E = 7.5$ keV. (a) Cooled from ODT at a rate of 0.05 °C/min, followed by an isothermal anneal at 215 °C for 6 days. (b) Direct anneal at 215 °C for 3 days. Major/minor tick marks denote 0.1/0.02° increments.

$a_1/a_2 = 1.154$ and $\phi = 54.7°$. Results for $T = 215$ °C ($\chi N \approx 60$) are presented as a function of the number of layers n, where parts b and c of Figure 4 show $a_1(n)/a_2(n)$ and $\phi(n)$, respectively. We find hexagonal packing in films one to three layers thick. At four layers, coexistence between hexagonal (majority) and orthorhombic symmetry is observed. This orthorhombic phase

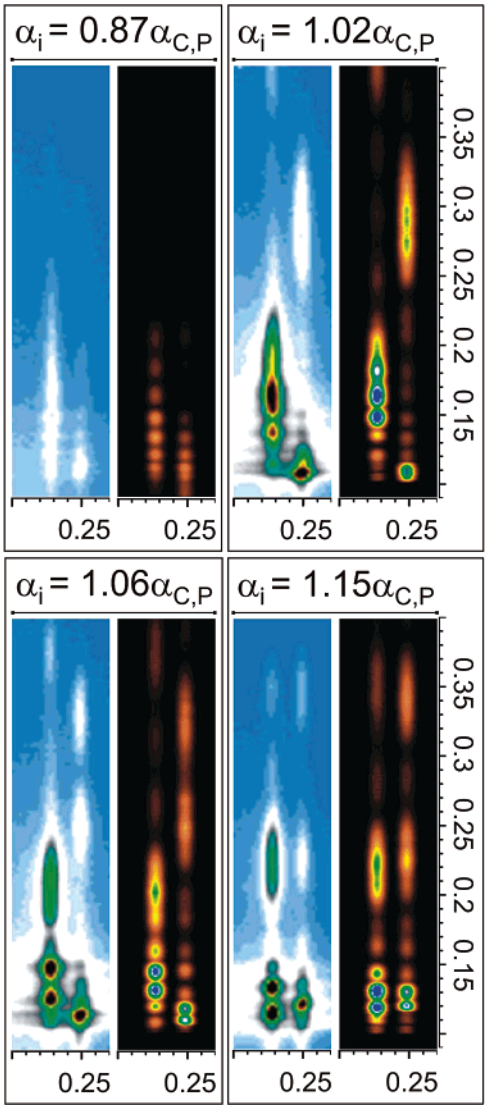

Figure 6. $n = 5$: Comparison between experimental (blue) and simulated $I(2\Theta,\alpha_f)$ data (black) with increasing α_i, assuming a face-centered orthorhombic symmetry. The incident angles marked for each pair denote the simulation angle, which is ~0.01° larger than the angle specified in the experiment. $E = 11.8$ keV. Major/minor tick marks denote 0.05/0.01° increments.

exhibits symmetry intermediate to that of the hexagonal lattice and the BCC (110) plane, characterized by $a_1(4)/a_2(4) \approx 1.08$ and $\phi \approx 57°$. As the number of layers is increased from 5 to a maximum of 23, a pure orthorhombic phase is measured, and the symmetry of the orthorhombic unit cell deforms to approach asymptotically $a_1/a_2 = 1.167$ and $\phi = 54.3°$. This limit resembles the BCC (110) plane stretched by 1% along the base of the unit cell b and compressed by 0.5% along the height of the unit cell h. To determine whether this apparent distortion is due to experimental error, the structure from a bulk sample was measured in transmission mode. The data points from the bulk sample are marked by the stars in Figure 4b−d and are consistent with a perfect BCC lattice, suggesting that the distortion measured in the limit $n \rightarrow 23$ is not an artifact. The data also show two interesting effects: First, the hexagonal unit cell stretches by 1% with increasing n in the range $n = 1-4$. Second, the nearest-neighbor spacing a_2 is constant in the range $n = 4-23$ where face-centered orthorhombic symmetry is observed. These results are shown in Figure 4d in terms of the normalized magnitudes $a_1(n)/a_1(3)$ and $a_2(n)/a_2(3)$.

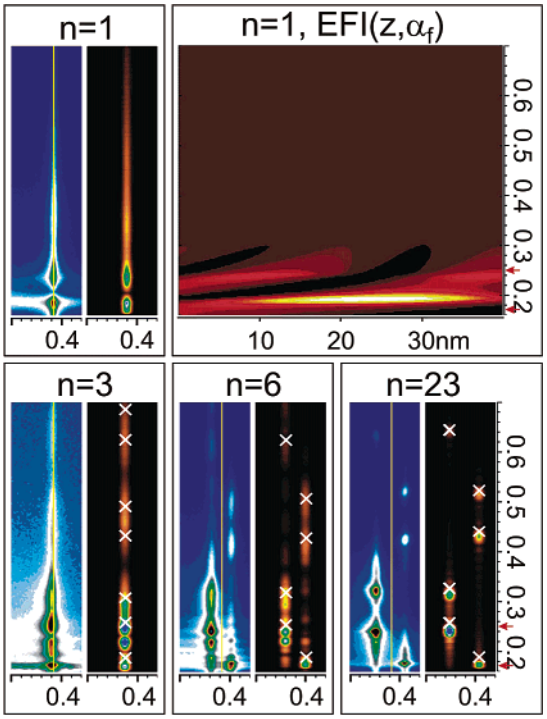

Figure 7. Comparison between experimental data (blue) and simulated $I(2\Theta,\alpha_f)$ data (black) at $\alpha_i = 1.03\alpha_{C,P}$, for $n = 1$, 3, 6, 23. Guidelines mark the position of the (10) reflection for $n = 1$. Red arrows on the left axis mark the critical angle of the polymer $\alpha_{C,P} \approx 0.17°$ and that of the silicon substrate $\alpha_{C,P} \approx 0.26°$. Top right: electromagnetic field intensity for a monolayer is shown as a function of the film depth z from the free surface at $z = 0$ and the out-of-plane diffraction angle α_f. $E = 7.5$ keV. Major/minor tick marks denote 0.1/0.02° increments.

With the exception of four layer films, all phases are independent of thermal history (circles/triangles denote direct anneal; diamonds/squares denote slow cooling from ODT at respective rates of 0.02 and 0.08 °C/min), indicating that these are equilibrium properties. The coexistence structure in films four layers thick suggests that the free energies of the HEX and orthorhombic phases are nearly degenerate. However, slow cooling from the bulk ODT at a rate of 0.05 °C/min followed by an isothermal anneal at 215 °C for 6 days produces an equilibrium hexagonal phase. These results are compared with the direct anneal at 215 °C for 3 days in Figure 5. Therefore, the orthorhombic phase at $n = 4$ is likely metastable.

Measurements from below (open symbols) and above (closed symbols) the critical angle of the polymer demonstrate that the structure is uniform throughout the depth of the film. There is no evidence of surface reconstruction like that postulated by Tan et al. in the weak segregation limit in the presence of a strong surface field.[26] However, they note that a weak surface field results in a direct transition to the BCC (110) plane, which is consistent with the results shown in Figure 4.

These in-plane symmetry results were reported in a recent letter along with a description of the transition based on a Landau-type self-consistent-field theory (SCFT).[1] The theoretical calculations, based on field theoretic simulations of monolayer and bulk free energies as a function of $1 \leq a_1/a_2 \leq 1.154$, demonstrate an abrupt transition from HEX to FCO packing at a discrete value of n^*. This symmetry breaking results from competition between the packing preferred at the surfaces with that preferred by the internal film layers. Theoretical results for $\chi N = 60$ suggest the transition to FCO occurs at $n^* = 7$, consistent with the experimental result of $n^* = 5$. The theoretical model does not capture the deviation from a perfect BCC lattice observed in the thickest films studied, where $a_1/a_2 > 1.154$ and $\phi < 54.7°$. To see whether the SCFT simulations can capture this effect would require a full 3D simulation of the multilayer film, which is too time-consuming to be practical at present.

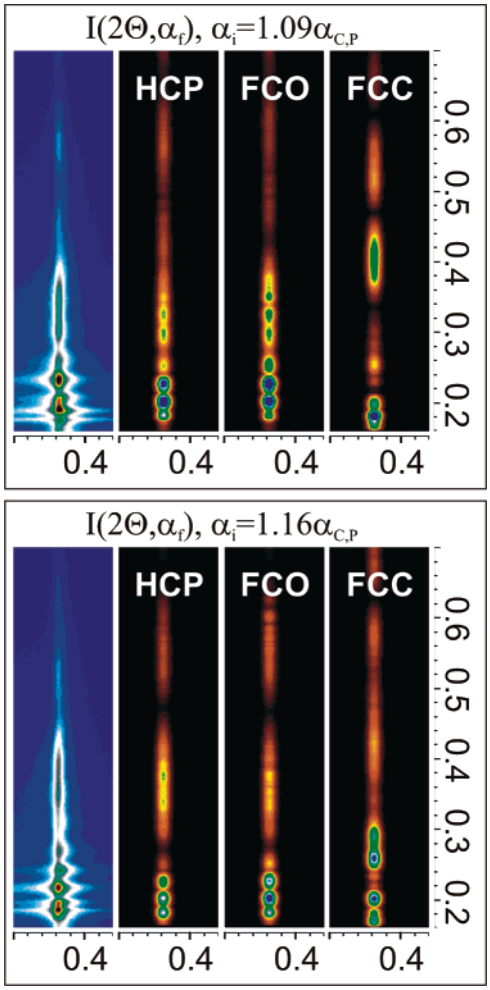

Figure 8. Comparison between experimental and simulated $I(2\Theta,\alpha_f)$ data for $n = 4$ with three assumed bases. $E = 7.5$ keV. Major/minor tick marks denote 0.1/0.02° increments.

Out-of-Plane Analysis and Space Group Assignment. The three-dimensional symmetry is determined by assuming a basis to describe stacking of the layers and then simulating the scattering in the DWBA framework to compare with the GISAXS measurements. As previously discussed, the incident angle α_i specified in the experiments is only accurate to within ~0.01°, which is problematic for two reasons: First, near the critical angle of the polymer, the depth sensitivity changes by 2 orders of magnitude over a range of <0.05°. Second, the position of the Bragg peaks in α_f is highly sensitive to the incident angle. Therefore, we compare several measurements collected over a range of α_i with a series of simulations to correct for the offset in incident angle and to verify the assumed basis. An example of this process is shown in Figure 6 for a five-layer-thick sample, where the simulations assume face-centered orthorhombic (FCO) symmetry, and we find excellent agreement between the calculated and experimental GISAXS patterns. Data collected below the critical angle of the polymer are not useful for analysis of the out-of-plane symmetry, but above the critical angle both experiments and simulations demonstrate the elongated Bragg peaks characteristic of scat-

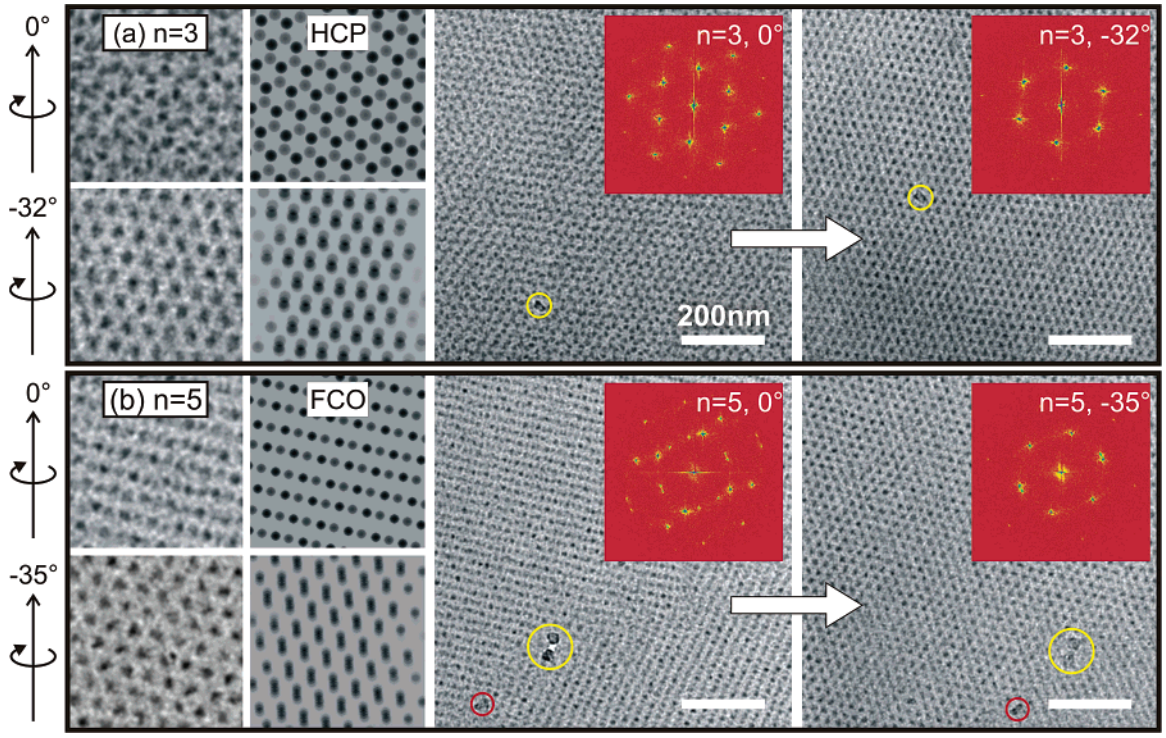

Figure 9. (a) TEM measurements for $n = 3$ at 0° and −32° and comparison with calculated projections for the HCP lattice. (b) TEM measurements for $n = 5$ at 0° and −35° and comparison with calculated projections for the FCO lattice. The dust particles used as reference markers are circled.

tering from thin films, which are the most useful feature for structural assignment.

Following this approach, the DWBA simulations demonstrate FCO symmetry in all films having 5−23 layers, a structure similar to the stacking of BCC (110) planes. Results for $n = 5$ and $n = 6$, 23 are shown in Figures 6 and 7, respectively. Scattering from films three to four layers thick, exhibiting hexagonal in-plane symmetry, is consistent with the hexagonal close-packed ABA lattice and inconsistent with close-packed ABC stacking of FCC (111) planes. Comparisons between experimental data and simulations based on HCP and FCC lattices are shown in Figure 8 for a four-layer sample. Also shown in Figure 8 are simulations based on FCO stacking with $a_1 = a_2$ and $\phi = 60°$, and this is indistinguishable from the HCP simulations.

A Comment on Standing Waves and Bragg Scattering in Thin Films. As previously outlined, scattering from thin films produces diffraction rods that are sharply peaked in-plane, and diffuse out-of-plane, where the intensity is a maximum at the Bragg point. This finite size broadening of Bragg peaks is inversely related to the number of unit cells perpendicular to the substrate, so as the number of layers is increased, the Bragg peaks become sharper in α_f. In GISAXS experiments, the diffuse scattering is amplified by coherent interference between the transmitted and reflected waves inside the film, an effect first noted by Yoneda.[23] These features are evident in Figure 7, which shows experimental and simulated GISAXS patterns for films 1, 3, 6, and 23 layers thick ($\alpha_i = 1.03\alpha_{C,P}$, $E = 7.5$ keV). The positions of the Bragg peaks, calculated by eqs 22−23, are marked by the white crosses on the simulated data. Peaks resulting from standing waves are identified by calculating the electromagnetic field intensity (EFI) inside the film from dynamical scattering theory.[24] For example, by eq 18, scattering from a monolayer does not produce an out-of-plane Bragg point, but the data for $n = 1$ show two peaks in the range $\alpha_{C,P} < \alpha_f < \alpha_{C,S}$. However, these maxima correspond with maxima in the EFI and are therefore assigned as peaks resulting from standing waves. The EFI for a monolayer is also shown in Figure 7.

TEM Results

The objective of TEM measurements is to assign a three-dimensional symmetry for samples having three and four layers, where analysis of the out-of-plane GISAXS data is inconclusive, and to verify the face-centered orthorhombic assignment for films having 5−23 layers. All samples were annealed by by slow cooling at a rate of 0.05 °C/min from 275 ± 5 °C through the bulk order−disorder transition of 250 ± 7 °C to 215 ± 5 °C, followed by a 4 day isothermal anneal at 215 ± 5 °C. Measurements of top-down (i.e., viewed perpendicular to the substrate) and tilted projections are compared with calculated projections for different lattice symmetries. The calculations assume perfect spheres having a radius of 7.5 nm and layer thickness $a_{layer} \approx 22$ nm. Results for films three to six layers thick are shown in Figure 9. For a three-layer film, the symmetry matches the hexagonal close-packed lattice. This is demonstrated in Figure 9a by measuring the structure at tilt angles of 0° and −32° and comparing with calculated projections. For a five-layer sample, the measured structure is predominantly the face-centered orthorhombic symmetry assigned by GISAXS simulations. Tilt projections for 0° and −35° are shown in Figure 9b. A very low density of close-packed stacking is measured in the five-layer samples (not shown), where these regions are only a few unit cells in diameter.

Top-down projections for films having four and six layers are shown in Figure 10a,b. Coexistence between HCP and FCO stacking is observed in four-layer films, where the HCP stacking is the majority. Six-layer samples demonstrate the FCO phase, and like the five-layer systems, a low density of close-packed structures is observed (not shown).

There is a narrow region of stability for close-packed spheres in the bulk phase diagram, where the FCC and HCP symmetries

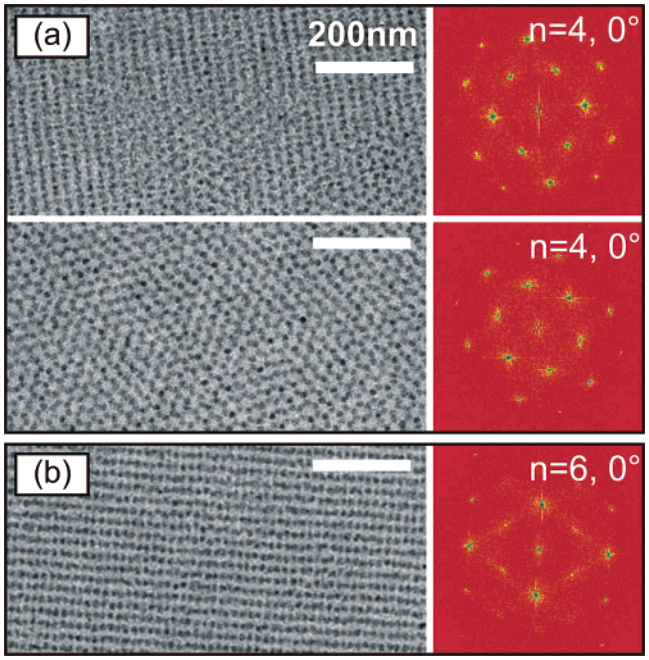

Figure 10. (a) Top-down projections for $n = 4$, showing (top) coexistence between HCP and FCO, and (bottom) pure HCP phase. (b) Top-down projection for $n = 6$, demonstrating FCO symmetry.

are predicted to have nearly degenerate free energies in strongly segregated systems. However, in more weakly segregated systems, the HCP arrangement is slightly favored over FCC.[27] In thin films, the internal bulklike layers influence the stacking sequence, so this may explain the stability of HCP over FCC in systems prepared near the order−disorder transition. There is one report of random stacking in three layer films of hexagonally packed poly(styrene-*b*-butadiene) spherical domains, also measured by TEM.[9] However, in this case the samples were annealed for very short times near the glass transition for the polystyrene majority component, so it is likely a nonequilibrium effect.

Conclusions

The transition from two- to three-dimensional packing in silicon-supported thin films of spherical-domain block copolymers is investigated with grazing incidence small-angle X-ray scattering and transmission electron microscopy. We find a discontinuous transition from close-packed hexagonal to face-centered orthorhombic packing as the number of layers is increased from four to five, where the face-centered orthorhombic phase is characterized by in-plane symmetry intermediate to that of the hexagonal lattice and the BCC (110) plane. As the number of layers is further increased from 5 to 23, the in-plane symmetry of the face-centered orthorhombic unit cell deforms to asymptotically approach that of a slightly distorted BCC (110) plane. These results are consistent with recent self-consistent-field theory simulations of spherical-domain block copolymers confined between hard boundaries, which predict a discontinuous transition from HEX to FCO packing at a discrete number of layers.[1]

Acknowledgment. We appreciate financial support from the NSF DMR Polymers Program, under Award DMR0307233. Use of the APS was supported by the U.S. DOE, Office of Science, Office of Basic Energy Sciences, under Contract DE-AC02-06CH11357. This work was partially supported by the NSF MRSEC under Award DMR05-20415. We thank R. A. Segalman for synthesis of the PS−PVP diblock copolymer utilized in this study and J. P. Lofvander for assistance with TEM.

References and Notes

(1) Stein, G.; Cochran, E.; Katsov, K.; Fredrickson, G.; Kramer, E.; Li, X.; Wang, J. Submitted for publication.
(2) Bates, F. S.; Fredrickson, G. H. *Annu. Rev. Phys. Chem.* **1990**, *41*, 525−557.
(3) Fasolka, M. J.; Mayes, A. M. *Annu. Rev. Mater. Res.* **2001**, *31*, 323−355.
(4) Koneripalli, N.; Singh, N.; Levicky, R.; Bates, F. S.; Gallagher, P. D.; Satija, S. K. *Macromolecules* **1995**, *28*, 2897−2904.
(5) Mayes, A. M.; Russell, T. P.; Bassereau, P.; Baker, S. M.; Smith, G. S. *Macromolecules* **1994**, *27*, 749−755.
(6) Matsen, M. W. *J. Chem. Phys.* **1997**, *106*, 7781−7791.
(7) Huinink, H. P.; Brokken-Zijp, J. C. M.; van Dijk, M. A.; Sevink, G. J. A. *J. Chem. Phys.* **2000**, *112*, 2452−2462.
(8) Karim, A.; Singh, N.; Sikka, M.; Bates, F. S.; Dozier, W. D.; Felcher, G. P. *J. Chem. Phys.* **1994**, *100*, 1620−1629.
(9) Henkee, C. S.; Thomas, E. L.; Fetters, L. J. *J. Mater. Sci.* **1988**, *23*, 1685−1694.
(10) Yokoyama, H.; Kramer, E. J.; Rafailovich, M. H.; Sokolov, J.; Schwarz, S. A. *Macromolecules* **1998**, *31*, 8826−8830.
(11) Radzilowski, L. H.; Carvalho, B. L.; Thomas, E. L. *J. Polym. Sci., Part B: Polym. Phys.* **1996**, *34*, 3081−3093.
(12) Thomas, E. L.; Anderson, D. M.; Henkee, C. S.; Hoffman, D. *Nature (London)* **1988**, *334*, 598−601.
(13) Matsen, M. W. *J. Phys.: Condens. Matter* **2002**, *14*, R21−R47.
(14) Thomas, E. L.; Kinning, D. J.; Alward, D. B.; Henkee, C. S. *Macromolecules* **1987**, *20*, 2934−2939.
(15) Yokoyama, H.; Mates, T. E.; Kramer, E. J. *Macromolecules* **2000**, *33*, 1888−1898.
(16) Parratt, L. G. *Phys. Rev.* **1954**, *95*, 359−369.
(17) Tolan, M. *X-ray Scattering from Soft Matter Thin Films*; Springer Tracts in Modern Physics 148; Springer-Verlag: Berlin, 1999.
(18) Lin, Y.; Boker, A.; He, J. B.; Sill, K.; Xiang, H. Q.; Abetz, C.; Li, X. F.; Wang, J.; Emrick, T.; Long, S.; Wang, Q.; Balazs, A.; Russell, T. P. *Nature (London)* **2005**, *434*, 55−59.
(19) Holy, V.; Pietsch, U.; Baumbach, T. *High-Resolut. X-ray Scattering Thin Films Multilayers* **1999**, *149*.
(20) Schmidbauer, M. *X-ray Diffuse Scattering from Self-Organized Mesoscopic Semiconductor Structures*; Springer Tracts in Modern Physics 199; Springer: New York, 2004.
(21) Lee, B.; Park, I.; Yoon, J.; Park, S.; Kim, J.; Kim, K. W.; Chang, T.; Ree, M. *Macromolecules* **2005**, *38*, 4311−4323.
(22) Robinson, I. K. *Phys. Rev. B* **1986**, *33*, 3830−3836.
(23) Yoneda, Y. *Phys. Rev.* **1963**, *131*, 2010−5.
(24) Narayanan, S.; Lee, D. R.; Guico, R. S.; Sinha, S. K.; Wang, J. *Phys. Rev. Lett.* **2005**, *94*, 145504.
(25) Guinier, A. *X-Ray Diffraction;* W.H. Freeman and Co.: New York, 1963.
(26) Tan, H. G.; Yan, D. D.; Shi, A. C. *Macromolecules* **2004**, *37*, 9646−9653.
(27) Matsen, M. W.; Bates, F. S. *Macromolecules* **1996**, *29*, 1091−1098. **Note Added in Proof:** While theory suggests that HCP is stable, recent experiments on bulk samples indicate that FCC packing is stable near the order−disorder transition for at least one diblock copolymer. Huang, Y.; Hsu, J.; Chen, H.; Hashimoto, T. *Macromolecules* **2007**, *40*, 406−409.

MA0625509